INTERNATIONAL JOURNAL FOR NUMERICAL METHODS IN FLUIDS
Int. J. Numer. Meth. Fluids 2005; **48**:455–466
Published online 11 March 2005 in Wiley InterScience (www.interscience.wiley.com). DOI: 10.1002/fld.964

A projection scheme for incompressible multiphase flow using adaptive Eulerian grid: 3D validation

T. Chen[1,‡], P. D. Minev[2,*,†] and K. Nandakumar[1,§]

[1]*Department of Chemical and Materials Engineering, University of Alberta, Edmonton, Alta, Canada T6G 2G6*
[2]*Department of Mathematical and Statistical Sciences, University of Alberta, Edmonton, Alta, Canada T6G 2G1*

SUMMARY

A three-dimensional finite element method for incompressible multiphase flows with capillary interfaces is developed based on a (formally) second-order projection scheme. The discretization is on a fixed (Eulerian) reference grid with an edge-based local *h*-refinement in the neighbourhood of the interfaces. The fluid phases are identified and advected using the level-set function. The reference grid is then temporarily reconnected around the interface to maintain optimal interpolations accounting for the singularities of the primary variables. Using a time splitting procedure, the convection substep is integrated with an explicit scheme. The remaining generalized Stokes problem is solved by means of a pressure-stabilized projection. This method is simple and efficient, as demonstrated by a wide range of difficult free-surface validation problems, considered in the paper. Copyright © 2005 John Wiley & Sons, Ltd.

KEY WORDS: finite element method; Navier–Stokes equations; free-boundary flows

1. INTRODUCTION

Multiphase flows offer many challenging problems to both theoreticians and developers of the next-generation algorithms. There are several popular numerical algorithms based on the Eulerian approach, which seems to be more convenient than the Lagrangian or Eulerian–Lagrangian approaches requiring frequent re-gridding that can hamper their efficiency. The reader is referred to the recent and comprehensive reviews by Tryggvason *et al.* [1] for the front-tracking method, Scardovelli and Zaleski [2] for the volume-of-fluid method and Osher and Fedkiw [3]

*Correspondence to: P. D. Minev, Department of Mathematical and Statistical Sciences, University of Alberta, Edmonton, Alta, Canada T6G 2G1.
†E-mail: minev@ualberta.ca
‡E-mail: tong.chen@ualberta.ca
§E-mail: kumar.nandakumar@ualberta.ca

Contract/grant sponsor: Natural Sciences and Engineering Research Council

Received 26 May 2004
Revised 17 January 2005
Accepted 21 January 2005

for the level-set method. Despite the difference in the interface description, there is a direct ideological relation among these methods in the sense that the governing systems are solved on a fixed grid. The difficulties of multiphase flow simulations in an Eulerian frame are due in part to the singularities (discontinuous pressure and normal derivatives of velocity) at a time-dependent free boundary. At present, the most popular way to deal with the singularities at the interface, particularly in the finite difference context, is the regularization of the δ-function using trigonometric approximation. The interface is no longer sharp but has a finite thickness over a few grid cells even though the interface might be tracked explicitly. However, such an approach results in costly computations because it is at best first-order accurate (in space) and it inherently reduces the accuracy of any formally higher-order scheme when the interfacial force becomes significant.

So far, the application of the finite element method (FEM) to free-boundary problems has been done almost exclusively in a Lagrangian framework (e.g. Reference [4]) or in an arbitrary-Lagrangian–Eulerian (ALE) framework (e.g. Reference [5]). The reader is referred to Cruchaga *et al.* [6] and the references therein for a brief review of the works with the ALE approach. The purely Eulerian approach was recently applied by Pillapakkam and Singh [7] and Quecedo and Pastor [8] for two-dimensional two-phase flows, directly extending the level-set method in the finite element context. Minev *et al.* [9] have presented a three-dimensional finite element technique based on a dynamic basis enrichment for the pressure and velocity in Taylor–Hood elements. With the Uzawa iteration method, the local correction of the approximations maintains a sharp interface over a fixed Eulerian mesh and hence, leads to a significant improvement of the mass conservation properties of the algorithm. An alternative approach using linear elements and a local h-refinement around the interface with a properly adapted projection scheme has been proposed by Chen *et al.* [10]. It captures the free boundaries with a level-set approach and then dynamically reconnects the surface of the front. The pressure approximation is discontinuous at the free boundaries which allows it to capture the pressure jump that occurs eventually there with an optimal accuracy. In the present paper, we validate the 3D version of this projection scheme using several free boundary incompressible flows which are known to be very hard for numerical simulation.

The rest of the paper is organized as follows. In Section 2, we present the mathematical formulation and a brief description of the discretization procedure, emphasizing on the details of the 3D extension. The validation examples are presented in Section 3. The conclusions are drawn in Section 4.

2. NUMERICAL TECHNIQUE

2.1. Formulation of the problem

We consider a three-dimensional flow domain $\Omega = \Omega_1 \cup \Omega_2$ that contains two different Newtonian fluids Ω_1 and Ω_2, with constant densities (ρ_1, ρ_2) and viscosities (μ_1, μ_2). The fluids are assumed to be homogeneous, immiscible and incompressible, and separated by a sharp interface $\Gamma = \partial\Omega_1 \cap \partial\Omega_2 \neq \varnothing$. In each single-phase subdomain $(i = 1, 2)$, the fluid motion is governed by the Navier–Stokes equations which, in a Cartesian coordinate system $\mathbf{x} = (x, y, z)$, read (in a stress-divergence form)

$$\rho_i[\partial_t \mathbf{u}_i + (\mathbf{u}_i \cdot \nabla)\mathbf{u}_i] = -\nabla P_i + \nabla \cdot \boldsymbol{\sigma}_i, \quad \nabla \cdot \mathbf{u}_i = 0 \quad \text{in } \Omega_i \tag{1}$$

where P_i is the hydrodynamic pressure, $\mathbf{u}_i$ is the velocity in the ith phase, $\mathbf{g}$ is the vector of gravitational acceleration, and $\boldsymbol{\sigma}_i = 2\mu_i\ \boldsymbol{\varepsilon}[\mathbf{u}_i]$ is the deviatoric stress with $\boldsymbol{\varepsilon}[\mathbf{u}_i] = \frac{1}{2}[\nabla\mathbf{u}_i + (\nabla\mathbf{u}_i)^{\mathrm{T}}]$ being the rate-of-strain tensor.

For simplicity, we assume Dirichlet boundary conditions on the external boundary $\partial\Omega$, $\mathbf{u}_i|_{\partial\Omega} = \mathbf{u}_{\mathrm{b}}$. Based on the classical hypothesis that the surface tension is proportional to the mean curvature κ of Γ, the force balance at the free boundary yields the well-known inter facial conditions

$$[-p\mathbf{I} + \boldsymbol{\sigma}]\mathbf{n} = -\gamma\kappa\mathbf{n} \tag{2a}$$

and

$$[\mathbf{u}] = \mathbf{0} \quad \text{on } \Gamma \tag{2b}$$

Here, $\mathbf{I}$ is the identity tensor. $[\cdot]$ denotes the jump of the corresponding quantity over Γ, $\mathbf{n}$ is the unit vector normal to Γ pointing towards Ω_1 from Ω_2, and γ is the surface tension coefficient. The mean curvature is given by $\kappa = \nabla\cdot\mathbf{n}$. This internal boundary condition clearly shows that both, the pressure and the normal derivative of the normal component of the velocity at the interface may have a jump discontinuity there. Therefore, the local grid refinement around it is essential for the proper approximation of the exact solution of the problem.

The fluid properties (ρ_i, μ_i) are identified using a smooth indicator function $\phi \in \Omega$ that satisfies the kinematic condition

$$\partial_t\phi + (\mathbf{u}\cdot\nabla)\phi = 0 \tag{3}$$

It is convenient if the fluid interface Γ corresponds to the $\phi = 0$ level of this function, so that

$$\mathbf{x} \in \begin{cases} \Omega_1 & \text{if } \phi(\mathbf{x}) > 0 \\ \Gamma & \text{if } \phi(\mathbf{x}) = 0 \\ \Omega_2 & \text{if } \phi(\mathbf{x}) < 0 \end{cases} \tag{4}$$

Then the normal direction to Γ is given by $\mathbf{n} = \nabla\phi/|\nabla\phi|$ at $\phi = 0$. This approach automatically takes care of merging and breaking of interfaces.

2.2. Discretization

For the details of the discretization procedure the reader is referred to Chen *et al.* [10]. It dynamically (at each time step) refines the grid only in the vicinity of the free boundaries, and uses a discontinuous pressure approximation there. One of the sets of pressure values at the free boundaries (on either side of the boundary) can be condensed using the interface boundary condition (2a). The discretization is performed by a formally second-order (in time) projection scheme, and a stabilized equal-order linear approximation in space. Here, we would like to comment specifically only on several important details of the implementation of the scheme in 3D.

2.2.1. Element refinement and reconnection around the front. We applied the local h-refinement technique [11] to the elements intersected by the front, and their immediate neighbouring elements of the basic reference mesh. It is an edge-based subdivision of a tetrahedron, very

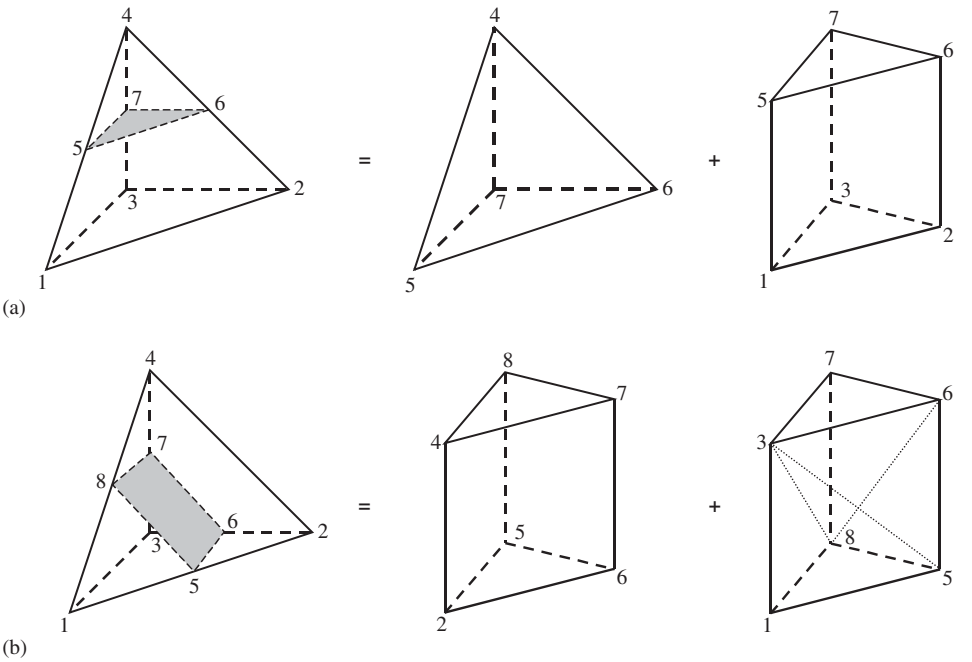

Figure 1. Reconnection of the front elements (pressure is double valued at intersection points 5, 6, 7, 8). The prism is further subdivided into three tetrahedra by linking the shorter diagonals of the quadrilateral faces.

fast for time-dependent problems if the permanent edge information is stored prior to the time marching. The refinement is conformal in the sense that all hanging nodes are avoided according to built-in templates for 11 basic configurations. The identification of the front elements in the reference mesh is straightforward because in such elements the level-set function ϕ has a different sign in the two vertices of at least three of their edges. The intersection points on these edges are determined by finding the zeros of the linear interpolant of ϕ on them. The piecewise linear approximation of the free boundary (a plane in each linear tetrahedron) is allowed to intersect a front element in only two basic configurations (see Figure 1). In case (a) the tetrahedron is sliced into one tetrahedron and one prism, while in case (b) it is sliced into two prisms. Each of the prisms can be further subdivided into three tetrahedra by using the better diagonal combinations of the quadrilateral faces without violating the connectivity rules. These two configurations are included in the built-in templates for the edge-based tetrahedron subdivision mentioned above. Since these are the two most common situations, the algorithm is much simplified if we do not allow the intersection points to coincide with a vertex of the front elements. This restriction is enforced in the following way. If the distance between the intersection point on an edge and its closest vertex is smaller than a preset minimum distance ε then this point is fictitiously moved away from the vertex (without resetting the values of ϕ) along the edge, so that the distance becomes equal to ε.

2.2.2. Reinitialization of the indicator function. After a sufficiently long time integration the numerical solution of the advection equation for ϕ can accumulate significant numerical dispersion which can in turn lead to a loss of stability of the overall scheme due to the essentially nonlinear condition (2a). Therefore, we need to occasionally reinitialize the indicator function ϕ. If $\{\mathbf{x}_\Gamma^i\}$ is the set of all (adapted) grid points at the time level of reinitialization which are on the free boundary then the indicator function is redefined by

$$\phi(\mathbf{x}) = \pm \min_i(|\mathbf{x} - \mathbf{x}_\Gamma^i|)$$

The sign is chosen depending on the phase which the point $\mathbf{x}$ is currently in.

Since this is not a very accurate measure for the distance between the point and the boundary, when we use it for the nodes close to the front ($|\phi(\mathbf{x})| < 2h$) we add more surface markers on the interface (we use the three Gaussian points on each of the triangular faces that mark the boundary).

The level-set function can also be reinitialized by solving the steady-state solution of the Hamilton–Jacobi equation [12]. We found that its solution on unstructured (tetrahedron) grids is non-trivial and the updated free boundary could be misplaced. One remedy to this problem is to prescribe/fix ϕ at the nodes of the front elements (e.g. Reference [8]). Unfortunately, these values are exactly the ones that need the reinitialization the most.

During the reinitialization of the distance function it is also convenient to correct the volume of the fluid particles because after a sufficiently long time integration their volume can be significantly changed. If V is the current volume of the particle and V^* is its correct volume then the volume-corrected level-set function is given by $\phi^* = \phi + (V - V^*)/S$, S being the surface of the particle as represented by ϕ. A similar idea is used by Tryggvason *et al.* [1] and their numerical examples indicate that the results are not altered significantly if the correction to ϕ is of order h^2. In the examples below, the reinitialization and the volume correction are performed every 20–100 time steps.

3. NUMERICAL EXAMPLES

3.1. Bubble expansion

We tested the proposed method with the growth of a submerged bubble pinned at an orifice and driven by a constant gas flow rate in an unbounded liquid. This process is often used for measuring of surface tension. Wong *et al.* [13] conducted an experimental study using silicone oil. They also performed numerical simulations with a boundary integral method in two-dimensional cylindrical coordinates. The Bond and capillary numbers in their study are defined as $Bo = \rho_1 g a^2/\gamma$, $Ca = \mu_1 Q/\gamma a^2$, respectively, where Q denotes the gas flow rate and a the inlet radius. The index 1 refers to the liquid. Here we consider the same flow at $Bo = 0.0945$ and $Ca = 1.55$ when both, the viscous and capillary forces are equally important. We solve the problem in a quarter of a cylindrical domain with a radius of 5 and a height of 8, as shown in Figure 2. The radius of the inlet is equal to 1. The inlet gas velocity is prescribed to be $\mathbf{u}_{\text{in}} = (0, 0, 1/\pi)$, and open boundary conditions at the top and full-slip boundary conditions on the cylindrical wall are prescribed. The density and viscosity ratios are $\rho_1/\rho_2 = 800$ and $\mu_1/\mu_2 = 200$. We initialize the bubble with a spherical cap of a height 0.25 in order to avoid having a zero initial volume. The reinitialization and the volume correction

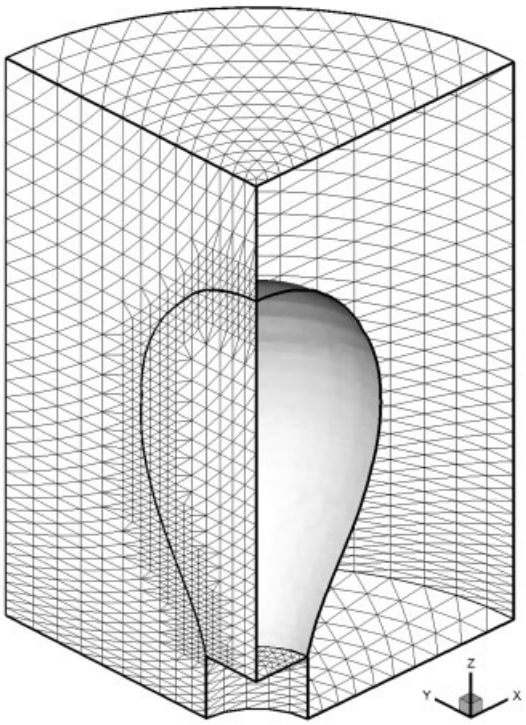

Figure 2. Domain triangulation for bubble expansion: basic reference mesh (nodes = 4599 and elements = 22 263) and dynamically refined reference mesh at $V = 60.0$ (nodes = 10 389 and elements = 54 510). The reconnection introduces additionally 3843 nodes on the front.

are performed at every 25 time steps ($\Delta t = 0.01$). The comparison of the computed results with the experimental measurements of Wong *et al.* [13] is shown in Figure 3. In Figure 4 we present the results for the same values of the parameters but with the orifice being tilted at an angle of 45°.

3.2. *Rising bubbles*

The terminal velocities and shapes of air bubbles rising in viscous fluids due to buoyancy have been a subject of many theoretical and experimental studies (see Reference [14]). An empirical correlation of the terminal rise velocity U of large single bubbles was proposed by Angelino [15]:

$$U = KV^m$$

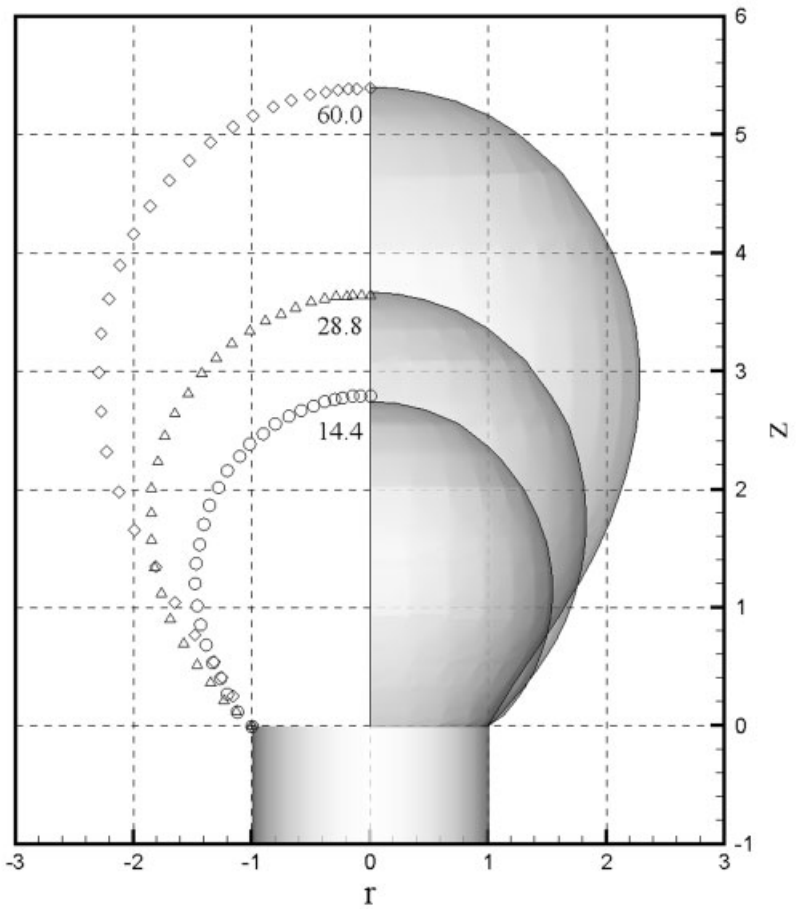

Figure 3. Comparison of numerical results with the experimental data of Wong *et al.* [13] for bubble expansion at $V = 14.4$, 28.8 and 60.0 ($Ca = 1.55$, $Bo = 0.0945$, left: experiments; right: present FEM results).

where $V = \pi d^3/6$ is the bubble volume, d is the volume-equivalent diameter, and

$$K = 25/(1 + 0.33Mo^{0.29})$$

$$m = 0.167(1 + 0.34Mo^{0.24})$$

where the Morton number is defined as $Mo = g\mu^4/\rho\gamma^3$.

Here we consider an air bubble with a diameter $d = 2.6$ cm, rising in two different liquids ($Mo = 345.9$ and 29.66). The problem is solved in a moving reference frame whose origin has a vertical coordinate equal to the corresponding coordinate of the centre of mass of the bubble (see Reference [10]). The density and viscosity ratios are set, respectively, to be

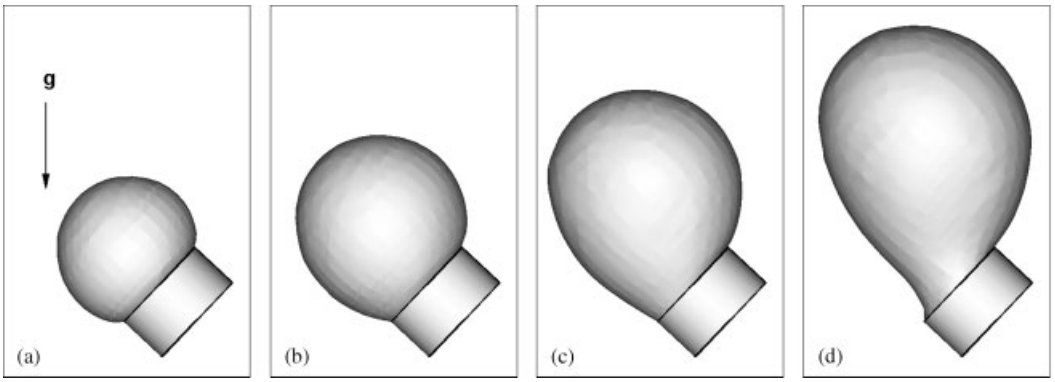

Figure 4. Bubble expansion from a tilted orifice at an angle of 45° (the parameters are the same as in the previous case).

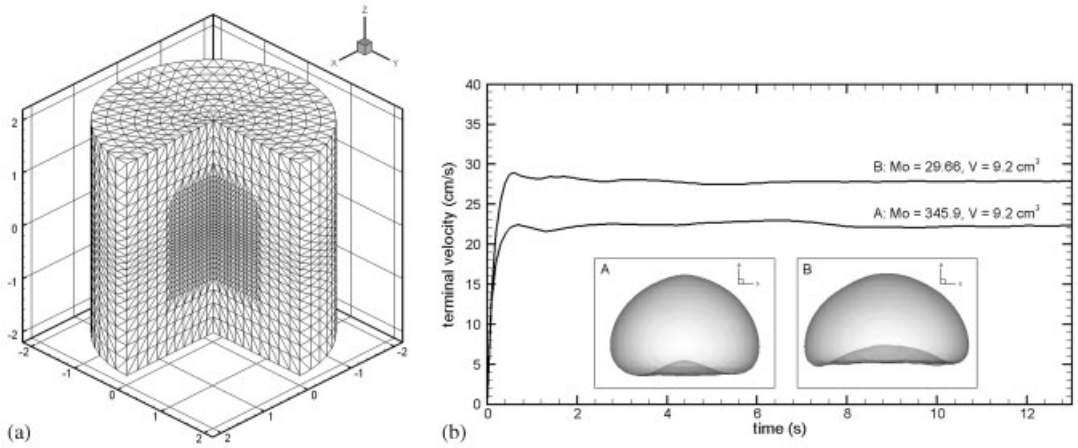

Figure 5. Air bubbles rising in viscous liquids: (a) basic reference mesh (nodes = 14 821 and elements = 84 366); and (b) time evolution of the centroidal velocities with corresponding terminal shapes.

$\rho_l/\rho_a = 1000$ and $\mu_l/\mu_a = 100$. The basic reference mesh is shown in Figure 5(a), and the solution domain is a cylinder with a diameter and a height both equal to $4d$. At the centre of the domain where the bubble is placed, the finite element grid is dynamically refined. The minimum grid size is about $d/25$ after the dynamic refinement. Full-slip boundary conditions are applied on the top of the cylinder, while open boundary conditions are imposed on the bottom. The evolution of the terminal velocities in the two cases described above are shown in Figure 5(b) with the corresponding terminal shapes being an oblate ellipsoidal cap. It is seen

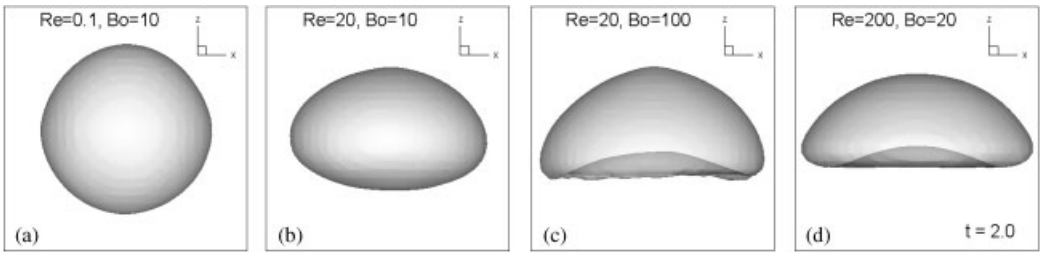

Figure 6. Predicted bubble shapes with various Reynolds and Bond numbers.

that after a quick acceleration, the velocities reach 22.30 and 27.87 cm/s, respectively. They are only about 3 and 9% different from the values computed using the empirical formula, which is within the error of the experimental data.

We further computed the terminal bubble shapes at various Reynolds and Bond numbers ($Bo = \rho g d^2/\gamma$). The results are presented in Figure 6 and qualitatively match the terminal shapes of Hua *et al.* [16] who used a two-dimensional axisymmetric front tracking/finite difference method. At $Re = 200$ and $Bo = 20$ (see Figure 6(d)) the bubble cannot reach a steady state and moves on a helical trajectory (see Figure 7). This is consistent with the experimental studies of Wu and Gharib [17].

Next, we evaluate the performance of the proposed method on a more complex problem, the rising and merging of air bubbles in a viscous liquid. We first consider two bubbles with the same radii R. Initially, the difference between the x coordinates of their centres is equal to R and the difference of their z coordinates is $2.3R$. This setting is the same as the one used by Sussman and Puckett [18], to simulate this flow at $\rho_1 = 1$, $\rho_2 = 0.05$, $\mu_1 = 0.0532$, $\mu_2 = 0.002$, $\gamma = 0.02$ and $g = 1$, which corresponds to the following dimensionless numbers: $We = 50$, $Fr = 1$ and $Re = 50^{3/4}$, based on the reference velocity $(Rg)^{1/2}$. The domain has a dimensionless size $4\times4\times8$, and the basic reference tetrahedral mesh contains $15\times15\times31$ nodes. Again, the resolution around the interfaces is doubled after one level of h-refinement in their vicinity. Symmetry boundary conditions are imposed on all vertical sides of the domain. The interaction of the two bubbles is presented in Figure 8, together with the velocity field and the pressure contours on the central plane $y = 0$. The non-axisymmetric merging of the two bubbles qualitatively agrees with the result of Sussman and Puckett [18], despite the fact that we used much lower (less than half of their) grid resolution.

Finally, a swarm of ten spherical bubbles was randomly generated in terms of the positions and radii ($0.8R$–$1.2R$). The parametric setting is the same as of the previous problem except for the Weber number which is equal to 1 and corresponds to a much larger surface tension coefficient. The computational domain is $8\times8\times10$ and it follows the vertical movement of the centre of mass of the bubble swarm. Open boundary conditions are imposed on the bottom, which eventually allows the bubbles to leave the domain freely. The basic reference mesh contains $31\times31\times39$ nodes. Figure 9 shows the shape evolution of the bubbles at the indicated time instances. The bubbles shapes are elliptical due to the strong surface tension, with the minor axis directed along the local tangent to the path. The centre of mass of the swarm has moved about $10.7R$ in the last frame ($t = 10.0$).

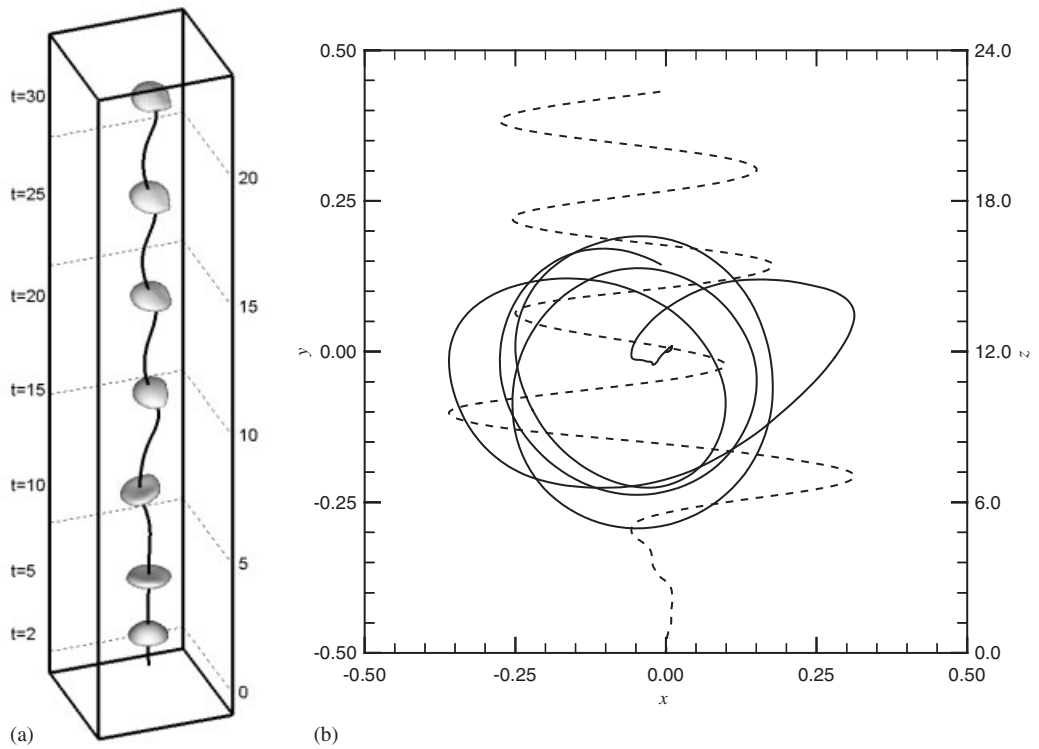

Figure 7. Path instability of a rising bubble ($Re = 200$, $Bo = 20$): (a) 3D trajectory; and (b) top (solid) and horizontal (dashed) views of the spiral motion.

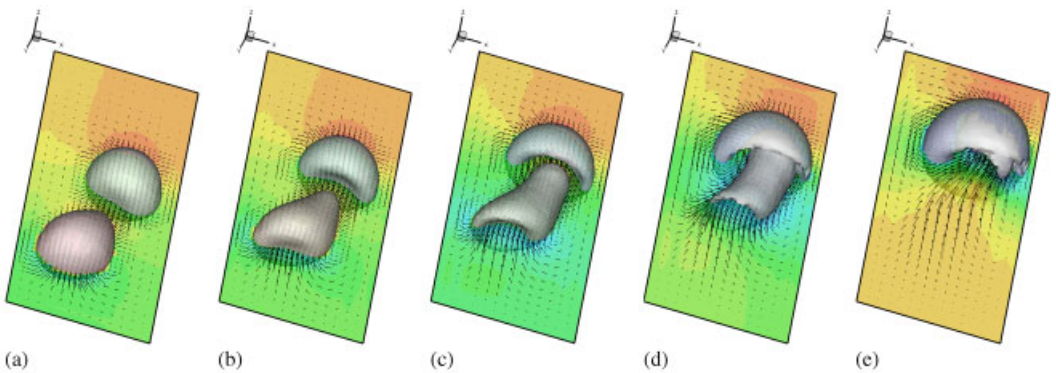

Figure 8. Non-axisymmetric merging of two viscous gas bubbles ($We = 50$, $Fr = 1$, $Re = 50^{3/4}$, $\rho_1/\rho_2 = 0$, $\mu_1/\mu_2 = 27$, basic reference grid $15 \times 15 \times 31$): (a) $t = 1.0$; (b) $t = 1.5$; (c) $t = 2.0$; (d) $t = 2.5$; and (e) $t = 3.0$.

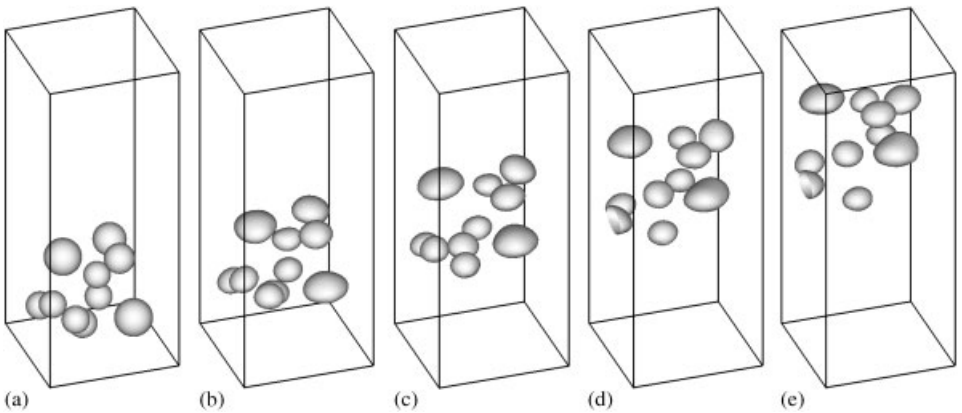

Figure 9. Rising of ten randomly generated viscous gas bubbles ($We = 1$, $Fr = 1$, $Re = 50^{3/4}$, $\rho_1/\rho_2 = 20$, $\mu_1/\mu_2 = 27$, basic reference grid $31 \times 31 \times 39$): (a) $t = 0.0$; (b) $t = 2.5$; (c) $t = 5.0$; (d) $t = 7.5$; and (e) $t = 10.0$.

4. CONCLUSIONS

A three-dimensional finite element method for incompressible multifluid flows with capillary interfaces, based on a formally second-order projection scheme has been validated in this paper. The validation examples include a wide range of sophisticated free-surface problems and are compared with available analytical and available numerical solutions. In this method, the fluid phases are advected and identified using a level-set method. The interfacial singularities are optimally approximated with a dynamic front reconnection technique. The accuracy of this method is improved using an edge-based local *h*-refinement around the interface prior to the reconnection of the front. The sophisticated and essentially unsteady and three-dimensional test problems considered in this paper clearly demonstrate the capabilities of the discretization technique.

ACKNOWLEDGEMENTS

This study was supported by research grants from the Natural Sciences and Engineering Research Council of Canada.

REFERENCES

1. Tryggvason G, Bunner B, Esmaeeli A, Juric D, Al-Rawahi N, Tauber W, Han J, Nas S, Jan YJ. A front-tracking method for the computations of multiphase flow. *Journal of Computational Physics* 2001; **169**:708–759.
2. Scardovelli R, Zaleski S. Direct numerical simulation of free-surface and interfacial flow. *Annual Review of Fluid Mechanics* 1999; **31**:567–603.
3. Osher S, Fedkiw RP. Level set methods: an overview and some recent results. *Journal of Computational Physics* 2001; **169**:463–502.
4. Shopov P, Minev PD, Bazhlekov I. Numerical method for unsteady viscous hydrodynamical problem with free boundaries. *International Journal for Numerical Methods in Fluids* 1992; **14**:681–706.
5. Chen T, Chwang AT. Trailing vortices in a free-surface flow. *Physics of Fluids* 2002; **14**:827–838.

6. Cruchaga M, Celentano D, Tezduyar T. A moving Lagrangian interface technique for flow computations over fixed grids. *Computer Methods in Applied Mechanics and Engineering* 2001; **191**:525–543.
7. Pillapakkam SB, Singh P. A level-set method for computing solutions to viscoelastic two-phase flow. *Journal of Computational Physics* 2001; **174**:552–578.
8. Quecedo M, Pastor M. Application of the level set method to the finite element solution of two-phase flows. *International Journal for Numerical Methods in Engineering* 2001; **50**:645–663.
9. Minev PD, Chen T, Nandakumar K. A finite element technique for multifluid incompressible flow using Eulerian grids. *Journal of Computational Physics* 2003; **187**:255–273.
10. Chen T, Minev PD, Nandakumar K. A projection scheme for incompressible multiphase flow using adaptive Eulerian grids. *International Journal for Numerical Methods in Fluids* 2004; **45**:1–19.
11. Ruprecht D, Heinrich M. A scheme for edge-based adaptive tetrahedron subdivision. In *Mathematical Visualization*. Hege HC, Polthier K (eds). Springer: Heidelberg, 1998; 61–70.
12. Osher S, Sethian JA. Fronts propagating with curvature dependent speed: algorithms based on Hamilton–Jacobi formulation. *Journal of Computational Physics* 1988; **79**:12–49.
13. Wong H, Rumschitzki D, Maldarelli C. Theory and experiment on the low-Reynolds-number expansion and contraction of a bubble pinned at a submerged tube tip. *Journal of Fluid Mechanics* 1998; **356**:93–124.
14. Bhaga D, Weber ME. Bubbles in viscous liquids: shapes, wakes and velocities. *Journal of Fluid Mechanics* 1981; **105**:61–85.
15. Angelino H. Hydrodynamique des grosses bulles dans les liquides visqueux. *Chemical Engineering Science* 1966; **21**:541–550.
16. Hua J, Lou J, Murali K, Lee KH, Kumar K. Simulation of bubble rise and deformation in liquid using a front tacking/finite difference method. In *Computational Technologies for Fluid/Thermal/Chemical Systems with Industrial Applications*, Kleijn CR, Kudriavtsev VV (eds). PVP-Vol. 424-2. ASME: New York, 2001; 225–234.
17. Wu M, Gharib M. Experimental studies on the shape and path of small air bubbles rising in clean water. *Physics of Fluids* 2002; **14**:L49–L52.
18. Sussman M, Puckett EG. A coupled level set and volume-of-fluid method for computing 3D and axisymmetric incompressible two-phase flows. *Journal of Computational Physics* 2000; **162**:301–337.

